# Detailed Simulation of Offshore Wind Turbine

Vladimir Leble, George Barakos*

*School of Engineering, University of Liverpool, Harrison Hughes Building*
*Liverpool, L69 3GH, U.K.*

**Abstract**

This paper presents results of numerical computations for floating off-shore wind turbines using, as an example, a machine of 10-MW rated power. The aerodynamic loads on the rotor are computed using the Helicopter Multi-Block flow solver developed at the University of Liverpool. The method solves the Navier-Stokes equations in integral form using the arbitrary Lagrangian-Eulerian formulation for time-dependent domains with moving boundaries. Hydrodynamic loads on the support platform are computed using the Smooth-ed Particle Hydrodynamics method, which is mesh-free and represents the water and floating structures by a set of discrete elements, referred to as particles. The motion of the floating offshore wind turbine is computed using a Multi-Body Dynamic Model of rigid bodies and frictionless joints. Mooring cables are modelled as a set of springs and dampers. All solvers were validated separately before coupling, and the results are presented in this paper. The importance of coupling is assessed and the loosely coupled algorithm used is described in detail alongside the obtained results.

*Keywords:* Offshore wind turbine, floating, CFD, SPH, multi-body, dynamics, HMB2

*Corresponding author
*Email address:* gbarakos@liverpool.ac.uk (George Barakos)
*URL:* https://www.liv.ac.uk/flight-science/cfd/off-shore-wind-turbines/ (George Barakos)

## 1. Motivation and objectives

| **Nomenclature** | |
|---|---|
| Latin | |
| $d$ | distance between the particles $[m]$ |
| $I$ | inertia tensor $[kg \cdot m^2]$ |
| $m$ | mass $[kg]$ |
| $w$ | relative weight between the fluid and body particles [-] |
| Greek | |
| $\alpha$ | artificial viscosity parameter [-] |
| $\gamma$ | adiabatic index [-] |
| Acronyms | |
| BEM | Blade Element Momentum method |
| BILU | Block-Incomplete Upper Lower factorisation |
| FOWT | Floating Off-shore Wind Turbine |
| FSI | Fluid Structure Interaction |
| GCG | Generalised Conjugate Gradient |
| GMRES | Generalised Minimal Residual method |
| HMB2 | Helicopter Multi-Block CFD Solver |
| HPC | High Performance Computer |
| IBQN-LS | Interface Block Quasi-Newton with an approximation for the Jacobian from a Least-Squares model |
| IQN-ILS | Interface Quasi-Newton algorithm with an approximation for the inverse of the Jacobian from a Least-Squares model |
| MBDM | Multi-Body Dynamic Model |
| MPI | Message Passing Interface library |
| SPH | Smoothed Particle Hydrodynamics Method |
| WT | Wind Turbine |

Wind is a substantial renewable energy source, and historical trends show the large development of on-shore wind turbine size and power capacity over the last three decades. However, high potential sites on land are already occupied, and others are hard to utilise due to e.g. difficult access, high altitude, costly transportation and on-site assembly. Therefore, a recent trend is to exploit the off-shore wind potential and take advantage of the available space and steady winds. Shallow water regions suitable for constructing seabed-fixed, off-shore wind turbines are also limited, and for sea depths exceeding 30-60 m, floating structures become more economic. Hence, emphasis is placed on the development of floating offshore wind turbines (FOWTs). Unlike onshore machines, the FOWT is a highly dynamic system since it is simultaneously subjected to the wind and wave loads and only constrained by a mooring system. Further, the rotor frequency is low due to the large size of the blades, and wave frequencies may come close or coincide with the rotational frequency of the rotor. It is, therefore, important to develop a method for the analysis of this air-structure-water system.

The common approach is to combine simplified tools into one hybrid model to predict wind turbine responses under wind and wave loads. The Blade Element Momentum (BEM) method is frequently used to calculate aerodynamic loads on the blades and tower (e.g. Jonkman, 2007; Skaare et al., 2007; Karimirad and Moan, 2013). Sometimes analytical models are used, that take the form of algebraic equations for the applied thrust that is proportional to the area of the rotor

and the relative velocity between the wind and the hub as in Roddier et al. (2009) and Karimirad and Moan (2012). Aero-elasticity is included in BEM methods, where the structure is described by a multi-body formulation in which wind turbine structures are subdivided into a number of bodies and each body consists of an assembly of Timoshenko beam elements (Larsen and Hanson (2007)). Another approach is to characterise flexible bodies using linear modal representation, which usually implies the assumption of small deflections.

The hydrodynamic loads on the support structure are often modelled with a linear potential theory assuming inviscid, incompressible and irrotational flow, also known as Airy wave theory (e.g. Jonkman, 2007; Roddier et al., 2009; Karimirad and Moan, 2013). In this case, frequency dependent hydrodynamic-added-mass and hydrodynamic-damping matrices, and wave-excitation force vector are precomputed for a given problem, and serve as an input to the coupled model. At the beginning of the computation, the wave-radiation-retardation kernel is obtained by integrating user-supplied added-mass or damping coefficients. This way external computer routines can be linked to the aerodynamic solver as a function, that employs convolution integrals and returns hydrodynamic loads at given instances. Since the equations are linear, the non-linear hydrodynamic viscous drag is included from Morison's equation using strip theory. Linearisation of the hydrodynamic problem implies that the translational displacements of the support platform are small relative to the size of the body, and that amplitudes of the incident waves are much smaller than their wavelengths *i.e.* steep or breaking waves can not be modelled.

Some extentions to the second-order potential flow was performed *e.g.* by Marino et al. (2011) and Roald et al. (2013). Even with second-order hydrodynamic terms included, however, the potential hydrodynamic theory might not completely apply to floating wind turbine platforms due to the large displacements encountered (Matha et al. (2011)).

Mooring lines constraining the FOWT are represented by springs (Savenije et al. (2010)), flexible beams (Skaare et al. (2007)) or multi-body chains of rigid bodies (Matha et al. (2011)). Sometimes, precomputed nonlinear force-displacement relationships are employed as in Karimirad and Moan (2012). Some of the works in the field of FOWT modelling are summarised in Table 1.

Table 1: Works relevant for the complete FOWT models.

| Author(s) | Aerodynamic method | Hydrodynamic method |
|---|---|---|
| Jonkman (2007) | BEM | Linear potential |
| Skaare et al. (2007) | BEM | Linear potential |
| Roddier et al. (2009) | Analytical | Linear potential |
| Karimirad and Moan (2013) | BEM/Analytical | Linear potential/Second-order potential/Morison's equation |

The purpose of this paper is to present a coupling algorithm that brings together two Naver-Stokes solvers. For this, the Helicopter Multi-Block (HMB2) solver developed at Liverpool University (Barakos et al. (2005)) is used to solve for the aerodynamic forces acting on the wind turbine (WT) blades. Hydrodynamic forces on the support platform are solved using the Smoothed Particle Hydrodynamics (SPH) method (e.g. Gomez-Gesteira et al., 2012; Woodgate et al., 2013). Both solvers are coupled by exchanging information while the FOWT is represented by a lumped mass model.

The remainder of the paper is organised as follows. First, the numerical solvers are described, and this is followed by validation cases for each one of them. Then, the coupling algorithm is described. Finally, test cases for the coupled computations are put forward, and results are presented and discussed before drawing conclusions.

## 2. Numerical methods

The HMB2 code is a 3D multi-block structured solver for the Navier-Stokes equations in 3D. HMB2 solves the Navier-Stokes equations in integral form using the arbitrary Lagrangian-Eulerian formulation for time-dependent domains with moving boundaries. The solver uses a cell-centred finite volume approach combined with an implicit dual-time method. Osher's upwind scheme (Osher and Chakravarthy (1983)) is used to resolve the convective fluxes. Central differencing (CD) spatial discretisation is used for the viscous terms. The non-linear system of equations that is generated as a result of the linearisation is solved by integration in pseudo-time using a first-order backward difference method. A Generalised Conjugate Gradient (GCG) method is then used (Eisenstat et al. (1983)) in conjunction with a Block Incomplete Lower-Upper (BILU) factorisation as a pre-conditioner. The HMB2 solver has a library of turbulence closures including several one- and two- equation models. Turbulence simulation is also possible using either the Large-Eddy or the Detached-Eddy simulation approach (Spalart et al. (1997)). The solver was designed with parallel execution in mind and the MPI library along with a load-balancing algorithm are used to this end. The flow solver can be used in serial or parallel fashion for large-scale problems. Depending on the purposes of the simulations, steady and unsteady wind turbine CFD simulations can be performed in HMB2 using single or full rotor meshes generated using the ICEM-Hexa tool. Rigid or elastic blades can be simulated using static or dynamic computations. HMB2 allows for sliding meshes to simulate rotor-tower interaction cases as described in Steijl and Barakos (2008). Alternatively, overset grids can be used with the details presented in Jarkowski et al. (2013). To account for low-speed flows, the Low-Mach Roe scheme (LM-Roe) developed by Rieper (2011) is employed for wind turbine cases (Carrión et al. (2013)).

The sea is modelled with the SPH method. Each SPH particle has individual material properties and moves according to the Navier-Stokes equations solved in the Lagrangian form. SPH offers a variety of advantages for fluid modelling, particularly those with a free surface and moving bodies. Due to the Lagrangian nature of the SPH method, the free surface requires no special treatment. Further, submerged bodies can be represented with particles. Therefore, it is natural for the method to include floating objects.

The motion of the FOWT components is computed with a multi-body model (MBDM) of rigid bodies and frictionless joints. Mooring cables are modelled as a set of springs and dampers, according to Savenije et al. (2010). The coordinate partitioning method of Nikravesh (1988) is used to solve the resulting system of mixed differential-algebraic equations. The time integration scheme is explicit and can be either the Runge-Kutta method of fourth order or Euler's method. The non-linear position equations are solved using the Newton-Raphson method with exact, an analytical, Jacobian.

Clearly, many disciplines converge in the coupled model of the FOWT. Current implementation is schematically presented in Figure 1.

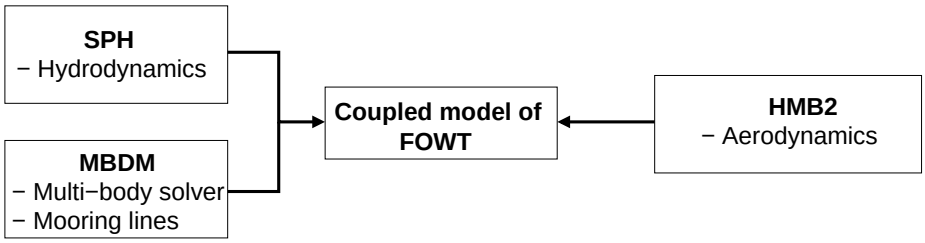


Figure 1: Schematic of the solvers employed in the floating off-shore wind turbine model.

### *2.1. Validation of the aerodynamic solver*

The HMB2 CFD solver has so far been validated for several wind turbine cases, including the NREL Annex XX experiments (Gómez-Iradi et al. (2009)), where the effect of the blades passing in front of the tower was captured, as can be seen by the deficit of the thrust values presented in Figure 2a. The pressure and PIV data of the MEXICO project (Carrión et al. (2014)) have also been used for validation, where the wake was resolved on a fine mesh capable to capture and preserve the vortices downstream the rotor (Figure 2b), which enabled the prediction of the onset of wake instabilities (Carrión et al. (2015)).

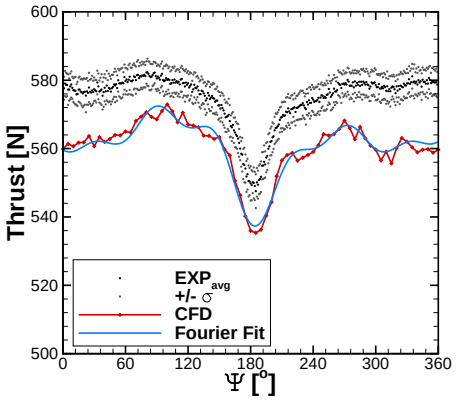


(a) Deficit in thrust of the NREL Annex XX blade when passing in front of the tower with corresponding Fourier series fit of five harmonics.

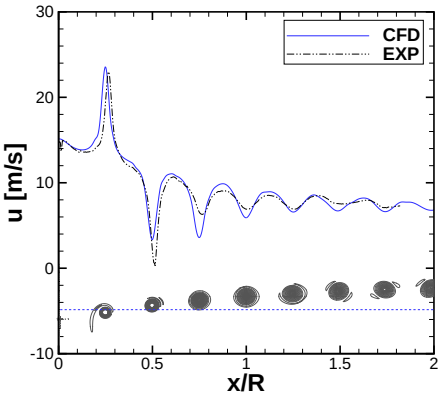


(b) Axial velocity profile passing through the first vortex generated by the MEXICO blade.

Figure 2: Validation cases for the HMB2 solver. **(a)** Thrust prediction over a full revolution of the NREL Annex XX wind turbine at 7m/s wind speed; **(b)** Prediction of MEXICO rotor wake, including axial velocity profile.

*2.2. Validation of the hydrodynamic solver*

The hydrodynamic loads are estimated using the SPH method validated against the experiments of Greenhow and Lin (1983) for the high speed entry of a half-buoyant solid cylinder into calm water. Following the experimental setup shown in Figure 3a, a cylinder of density of $500kg/m^3$ was allowed to fall freely from the height of $0.8m$ under gravity acceleration; the water depth was $0.3m$. The density of the cylinder was assigned by defining the relative weight between fluid and cylinder particles to be $w = 0.5$. Simulations were run with a cubic spline kernel, artificial viscosity with viscosity parameter $\alpha = 0.1$, adiabatic index $\gamma = 7$, and Courant-Friedrichs-Lewy number $CFL = 0.2$. The viscosity between the cylinder SPH particles and fluid particles was neglected. Five cases were compared with different distances $d$ between the particles. The penetration depth of the cylinder for all cases along with experimental results are shown in Figure 3b, whereas Figure 4 shows the water surface deformation. The results were used for estimating the particle density and viscosity necessary for computations of floating bodies. Note, that the best agreement with the experiment was obtained with distances between the particles $d = 0.23cm$, what corresponds to 25 particles per radius of the cylinder.

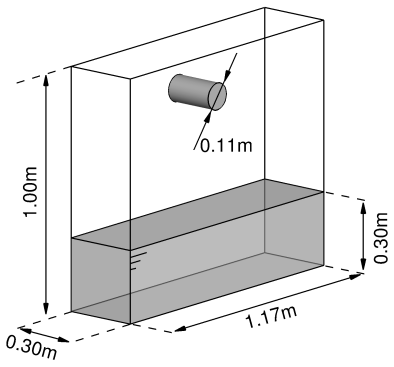


(a) Schematic of the SPH validation setup.

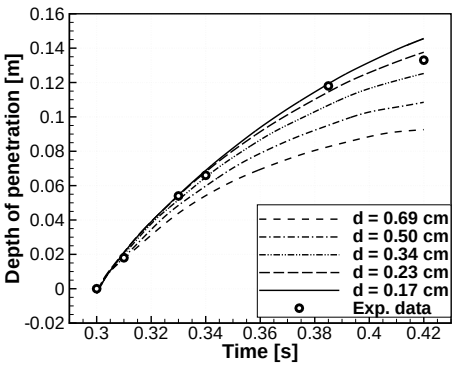


(b) Depth of penetration of a cylinder.

Figure 3: Validation case for the SPH solver. (a) Schematic of the SPH validation setup; (b) Depth of penetration of a cylinder of density 500 kg/m$^3$: SPH results for different distances between particles ($d$); and (c) experimental results of Greenhow and Lin (1983).

*2.3. Validation of multi-body dynamics solver*

The MBDM was validated using simple mechanical systems of known solution as presented in Haug (1989) like 2D and 3D slider-crank mechanisms. A 2D slider crank mechanism consists of a ground, crank, arm and slider bodies with properties summarised in Table 2. Although the configuration of the mechanism is planar, the employed bodies are three dimensional. The slider moves in the compression chamber, as shown in Figure 5b. As the slider moves to the inside of the chamber, a resisting force due to compression of the gas acts on the slider. This force increases until the exhaust valve opens. Equation 1 defines the gas force $F_C$ on the slider during the compression, that is, when $\dot{x}_3 > 0$. At $x_3 = 5m$, the valve opens. During the intake stroke, no

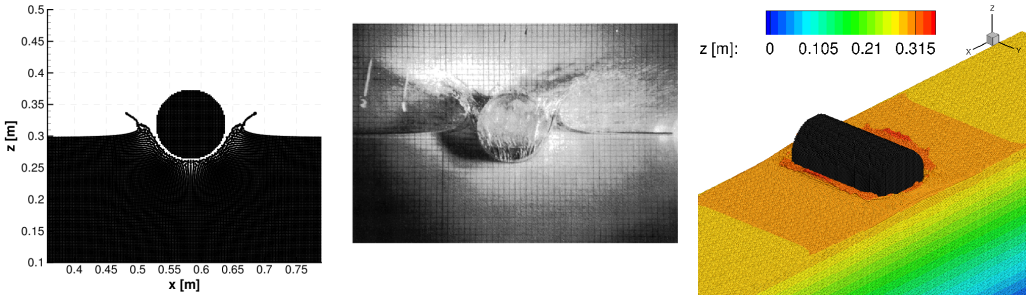


(a) Cross section view. (b) Experiment. (c) Isometric view.

Figure 4: Surface deformation during water entry of a cylinder for time $t = 0.32s$ from the beginning of the fall. Comparison between CFD results with distance $d = 0.23m$ between particles and experimental results by Greenhow and Lin (1983).

gas force acts on the slider.

$$F_C = \begin{cases} -\frac{282857}{6-x_3} + 62857, & 1.5 \leq x_3 \leq 5 \\ -11 \cdot 10^4[1 - \sin(2\pi(x_3 - 5.25))], & 5 < x_3 \leq 5.5 \end{cases} \tag{1}$$

Figure 5(c) shows the gas force as a function of the position and velocity of the slider.

Table 2: Properties of the bodies employed to represent the 2D slider-crank mechanism for dynamic analysis.

| Name | Mass $[kg]$ | Inertia tensor $[kg \cdot m^2]$ |
|---|---|---|
| Crank | 200 | $\begin{bmatrix} 450 & 0 & 0 \\ 0 & 450 & 0 \\ 0 & 0 & 450 \end{bmatrix}$ |
| Rod | 35 | $\begin{bmatrix} 35 & 0 & 0 \\ 0 & 35 & 0 \\ 0 & 0 & 35 \end{bmatrix}$ |
| Slider | 25 | $\begin{bmatrix} 0.02 & 0 & 0 \\ 0 & 0.02 & 0 \\ 0 & 0 & 0.02 \end{bmatrix}$ |
| Ground | 1 | $\begin{bmatrix} 1 & 0 & 0 \\ 0 & 1 & 0 \\ 0 & 0 & 1 \end{bmatrix}$ |

To match the conditions used by Haug (1989), the gravitational force was acting in the positive $x$ direction. The initial orientation of the crank was set to $\phi(0) = \pi$ and the initial angular velocity of the crank was set to $\dot{\phi}(0) = 30rad/s$. The followed notation is as shown in Figure 5a. A constant torque of $41,450Nm$ was applied to the crank, and results are presented in Figure 6. The integration scheme employed for this computation is the Runge-Kutta method of fourth order, with time step chosen as $\Delta t = 0.001s$.

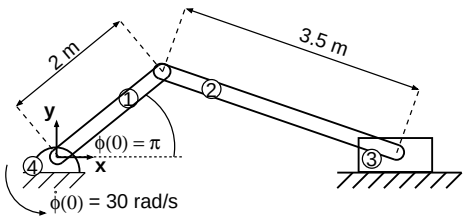


(a) Schematic representation of slider-crank mechanism.

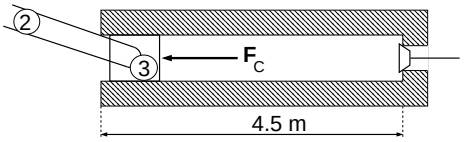


(b) Slider in a compression chamber.

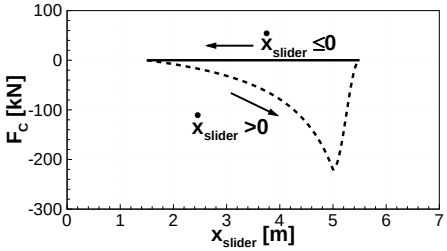


(c) Gas force versus slider position.

Figure 5: Validation case for the MBDM solver - dynamic analysis of the 2D slider-crank compressor mechanism.

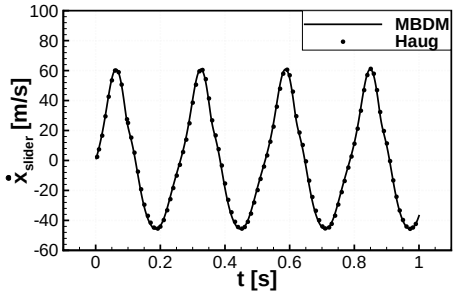


(a) Velocity of the slider.

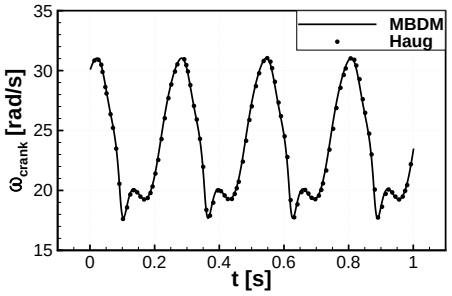


(b) Rotational velocity of the crank.

Figure 6: Comparison between velocity in $x$ direction of the slider, and rotational velocity of the crank for the MBDM code and results obtained by Haug (1989).

*2.4. Coupling algorithms*

Coupling algorithms were studied extensively for the past three decades. Coupling problems arise in many multi-physic phenomena, like fluid-structure interaction (FSI), but can also result from domain decomposition, where each sub-domain employs different discretisation or is solved with different method (Zienkiewicz O.C. et al. (2005)). The multi-physics problem with adjacent domains can be simulated in a monolithic or in partitioned way. The former refers to the flow equations and structural equations being solved simultaneously, while the latter means that they are solved separately. The monolithic approach requires a specific solver for the particular combination of physical problems, whereas the partitioned approach allows for solver modularity. Moreover, the partitioned approach allows to solve the fluid equations with different techniques developed specifically for the air and water. Further, this approach reduces the computational complexity per time-step, simplifies explicit/implicit treatment, facilitates sub-cycling, and eases replacements when better mathematical models and methods emerge in the fluid sub-disciplines. On the other hand, the partitioned simulation requires a special treatment to account for the interaction between the involved domains. Hence, computational efficiency over a monolithic approach is not necessarily guaranteed (Fellipa C.A. et al. (1999)). The monolithic solution - which is the ultimate form of strong coupling, does not recognise the differences between the mathematical properties of the subsystems. Furthermore, it tends to ignore the issues of software modularity, availability, and integration, even though each of these issues can be in practice a major obstacle (Farhat C. et al. (2006)). Considering that two available and validated solvers (HMB2 and SPH) can be used in this work, the emphasis is placed on partitioned algorithms.

Partitioned coupling can be weak or strong. Explicit algorithms are weak (or loose) as the solvers exchange information once per time step, and the coupled equations are not exactly satisfied due to explicit treatment. Depending on the formulation, one side of the coupling boundary conditions is usually lagging behind another. This can be improved with staggering or extrapolation techniques, but the scheme remains weak, and coupling errors may be introduced. However, loosely coupled algorithms are attractive, since among all solution methods, they are the simplest to implement for realistic applications, and the most computationally inexpensive per time step.

Implicit algorithms are strong (or tight), and enforce exactly the coupling conditions at each time level. This is obtained by conducting iterations until boundary equations are satisfied to certain, prescribed accuracy. The coupling problem can be formulated either as fixed-point or root-finding problem. For the former, fixed-point Jacobi or Gauss-Seidel methods can be employed. Although easy to implement, those methods converge slowly if at all. Under-relaxation techniques can be used to improve convergence of the fixed-point iterations. Methods like fixed under-relaxation, adaptive Aitken's under-relaxation or steepest descent relaxation are some of the possible choices (e.g. Kttler and Wall, 2008; Degroote et al., 2010). Newton's method can also be used. This method requires Jacobians relating the solutions of both solvers, that are usually not known. This can be circumvented by employing approximation of Jacobian or Jacobian-vector product. Those type of coupling methods are called Quasi-Newton. Recently, new strongly coupled algorithms have been proposed.

Vierendeels et al. (2007) proposed an Interface Quasi-Newton algorithm with an approximation for the inverse of the Jacobian from a Least-Squares model (IQN-ILS). This approach was further investigated by Degroote et al. (2010), where they compared its performance with the Interface Block Quasi-Newton with an approximation for the Jacobian from a Least-Squares model (IBQN-LS), Aitken relaxation, and the Interface Generalised Minimal Residual method (Interface-GMRES(R)) algorithms. Demonstrated results showed that IQN-ILS and IBQN-LS

performed similarly, using 3 times less evaluations and converging 4 times faster than the Aitken's relaxation method. IQN-ILS and IIBQN-LS were also found to use 2 times less evaluations and be almost 3 times faster than the Interface-GMRES algorithm.

Fernández and Moubachir (2005) reformulated fluid-structure interaction as a non-linear problem in the state of the structure, with the flow states considered as internal variables of the problem. This system was subsequently solved with the Newton-Raphson method using an exact Jacobian. The performance of this algorithm was compared with the performance of the Aitken relaxation and Quasi-Newton GMRES methods, for the inviscid flow in an elastic tube. Results showed that Aitken's relaxation was twice as slow as the Quasi-Newton and the exact Jacobian methods, and required almost 40 times more iterations. Further, for time steps of $\Delta t = 10^{-4} s$, both latter algorithms showed similar behaviour in convergence. However, for time steps of $\Delta t = 10^{-3} s$, the fixed-point and Quasi-Newton algorithms failed to converge. This implies sensitivity of the methods to the employed Jacobian.

The strong coupling may be important if the phenomena occurring in both fluids have similar time scales. Due to frequency similarities, resonances may occur and the exact response of a system will deviate from what is predicted by a loosely coupled algorithm. On the other hand, if time scales are largely different, loosely coupled algorithm may be sufficient. The exact bounds when the strong coupling is required for particular FOWT must be carefully assessed. Some indication comes from the waves and rotor frequency analysis. The sea state, wave height, wave frequency, and wind speed are empirically related in terms of range and most probable values *e.g.* in Lee et al. (1985). On the other hand, every wind turbine is designed to operate at a particular rotational frequency for a given wind speed. This allows to construct a "Campbell" diagram for the FOWT investigated in this work (Figure 7). It is clear, that for sea states between 3 and 4 (or wind speed about $9 m/s$) resonances may occur. The rated power production for this 10-MW FOWT corresponds to the wind speed of $11.4 m/s$, or sea state 4. This indicates, that for rated conditions, the weakly coupled algorithm may be sufficient.

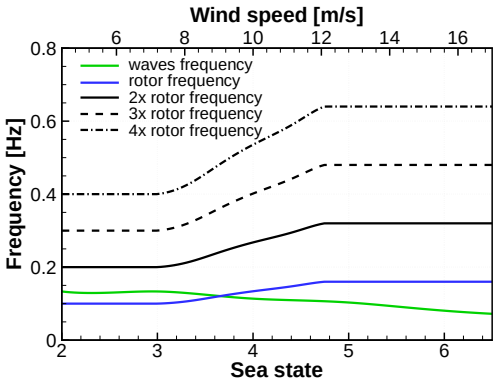


Figure 7: Campbell diagram for the investigated FOWT showing frequencies of the rotor and the waves as function of sea state and wind speed.

### *2.5. Coupling scheme and its implementation*

In general, the exchange of information without stopping the computations can be implemented in three ways: through files, shared memory or the Message Passing Interface (MPI).

Writing a file is the simplest solution. Both solvers can be launched separately and write files whenever exchange of information is required. This approach calls for very minor changes to both codes. The drawback is that writing and reading from hard drive creates a bottleneck, and slows down the computation especially if information is exchanged often, and large amount of data is to be exchanged.

In the shared memory approach multiple processes have access to the same memory, allowing them to change it and read changes made by other processes. If the random access memory (RAM) is to be used, it requires a shared memory machine, which may not be available on a general High Performance Computer (HPC). The file system can be used instead by mapping the memory on the hard drive. This approach suffers from the same drawback as the case of writing files.

Both employed CFD solvers are parallelised using MPI and the Single Program, Multiple Data (SPMD) paradigm, where each instance of the solver is assigned to perform the same task on different sets of data. Therefore, the easiest way to combine solvers is to employ MPI, but in Multiple Program, Multiple Data (MPMD) approach, where different programs operate on different sets of data. However, direct MPMD implementation of SPMD solvers requires additional effort to split the global communicator, such that each of the solvers is in a separate communicator (*MPI_COMM_WORLD*) with a separate ordering of precesses, as detailed in Open MPI (2015). This can be avoided by dedicating one process to be in charge of executing both solvers with *MPI_Comm_spawn* routine. The dedicated code is referred to as master program or parent, and spawned processes are referred to as children. This approach has number of advantages briefly summarised as:

1. Spawned program has its own *MPI_COMM_WORLD*, therefore no modifications are required to original code with respect to processes that are going to communicate inside the child group.
2. Ordering of the processes is separate for parent and children. This way no modifications are required to original code with respect to process that is going to be in charge of the computation inside the child group.
3. Child process can easily identify if it was spawned or launched directly with MPI command. This maintains the original code functionality.

In the present work, the communication between the solvers was established through the Message Passing Interface (MPI), where the MBDM is executed as a single process and is dedicated to start SPH and HMB2 parallel solvers. The data flow diagram of the implementation is presented in Figure 8. The communication was validated by executing separately SPH or HMB2, and comparing with the results were the body motion was introduced by MBDM. Due to the Lagrangian nature of the SPH method, the submerged bodies can be represented with particles and do not require specific coupling. Therefore, by utilising MPI, the MBDM substituted the body motion routines of the SPH solver and reduced the number of coupled codes to two - SPH and HMB2. This implies that MBDM is advancing in time with the same integration scheme as SPH using a symplectic method in this case (Leimkuhler et al. (1996)).

In the present paper, a weakly coupled approach is employed, namely the parallel conventional staggered method shown in Figure 9. Both solvers are advancing with different but constant time steps. SPH employs a time step of $\Delta t_{SPH} = 2 \cdot 10^{-4} s$ with $CFL = 0.2$, whereas HMB2 employs a time step of $\Delta t_{HMB2} = 2 \cdot 10^{-2} s = 100 \Delta t_{SPH}$ with implicit $CFL = 5.0$. The small time step for the SPH method is required by the explicit integration scheme. The HMB2 solver

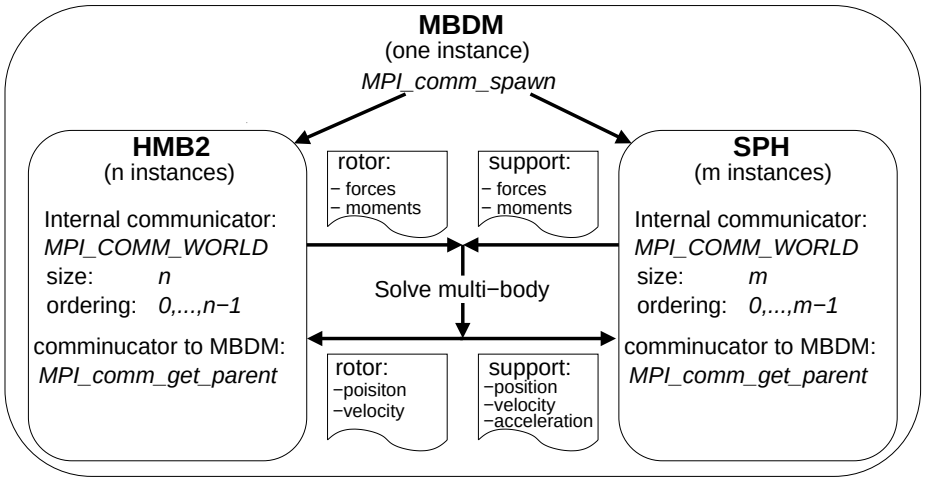


Figure 8: Flow chart of the MPI implementation and data exchange for coupled model.

employs an implicit dual-time method by Jameson (1991) that is superior for larger time steps. Synchronisation of the solvers is performed at the end of each HMB2 step.

At the beginning of each synchronisation time step, the position and velocities of the rotor are transferred to the HMB2 aerodynamic solver, and forces and moments on the rotor are passed to the SPH. The two solvers are then advancing to a new time level with different methods and different number of steps. SPH performs 100 symplectic steps, while HMB2 performs 350 implicit pseudo-time steps. During the symplectic steps of the SPH code, the aerodynamic loads are kept constant (frozen). In return, the position and velocities of the rotor are kept constant during the implicit steps of HMB2. Once the synchronisation point is reached, the new position and velocities of all bodies, and rotor loads are obtained. Then, the algorithm proceeds to the new time level and information between the solvers is exchanged.

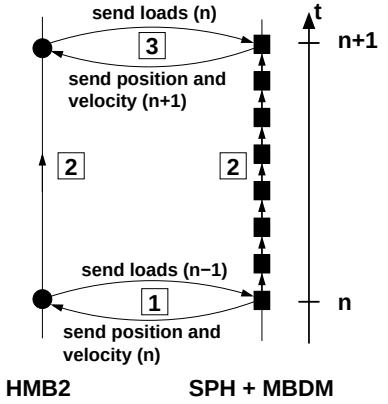


Figure 9: The parallel conventional staggered method employed in present work.

## 3. Test case description

A 10-MW wind turbine design by Bak et al. (2013) is used in this work. The rotor diameter is 178.3$m$, and the wind turbine operates at a wind speed of 11$m/s$ with a rotational speed of 8.8$rpm$. The blades have a pre-coning of 2.5° and nonlinear pre-bending with 3.3$m$ displacement at the blade tip.

The wind turbine is attached to the floating support which consists of three cylindrical floats that increase the buoyancy and stability of the structure. A similar concept of the support platform was investigated by Roddier et al. (2009). Unlike that design, the present support is simplified to be symmetric with respect to the location of the tower and the floats are connected to the base of the tower with a solid frame. The size of the tower is taken from Bak et al. (2013), and the dimensions of the support were calculated to provide sufficient buoyancy. A schematic of the studied FOWT is shown in Figure 10.

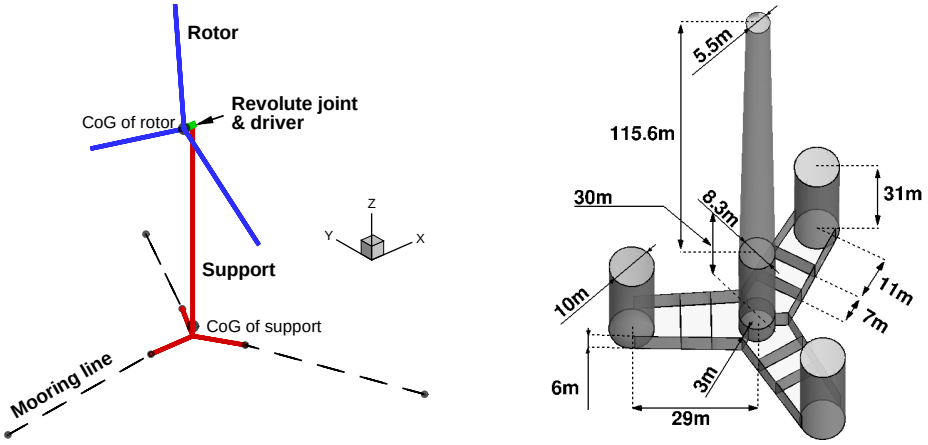


(a) Schematic of the MBDM model of FOWT.

(b) Dimensions of the support and tower.

Figure 10: Schematic of the employed model of FOWT (a), and dimensions of the semi-submersible support and tower (b). FOWT model consists of three mooring lines and two rigid bodies: the rotor (blue) and combined body representing nacelle, tower and support (red).

In the present model, the FOWT is represented by three mooring lines and two bodies, as shown in Figure 10a. The first body represents the rotor (three blades with the spinner), and the second body represents the combined nacelle, tower and floating support rigidly linked to each other. The two bodies are connected by a revolute joint and a constraint of constant rotational speed is applied to the rotor. The resulting system has 6 unconstrained degrees of freedom. The mechanical properties of the bodies and mooring lines are presented in Table 3.

The FOWT is placed in a shallow tank of length 500$m$, width 150$m$ and height 30$m$. The tank is filled with water to a depth of 20.6$m$. The waves are generated using a paddle on one side, and dissipated using a beach-like slope on the other side of the tank. The tank is presented in Figure 11. Waves are generated to represent the specific sea state corresponding to a given wind speed. Based on the measurements of annual sea state occurrences in the North Atlantic and North Pacific (Lee et al. (1985)), the wind speed of 11$m/s$ corresponds to a sea state 4 with a mean wave height of 1.88$m$ and a period of 8.8$s$.

Table 3: Mechanical properties of the employed bodies and mooring lines.

| | |
|---|---|
| **Rotor** | |
| m $[kg]$ | $227,962$ |
| I $[kg \cdot m^2]$ | $\begin{bmatrix} 1.56 \cdot 10^8 & 0 & 0 \\ 0 & 7.84 \cdot 10^7 & 0 \\ 0 & 0 & 7.84 \cdot 10^7 \end{bmatrix}$ |
| **Nacelle, support and tower** | |
| m $[kg]$ | $4,223,938$ |
| I $[kg \cdot m^2]$ | $\begin{bmatrix} 2.03 \cdot 10^{10} & 0 & 0 \\ 0 & 2.03 \cdot 10^{10} & 0 \\ 0 & 0 & 2.81 \cdot 10^9 \end{bmatrix}$ |
| **Mooring lines** | |
| 120.0 | Angle between adjacent lines $[°]$ |
| 20.6 | Depth of anchors below SWL $[m]$ |
| 7.0 | Depth of fairleads below SWL $[m]$ |
| 116.73 | Length of the relaxed line $[m]$ |
| $400 \cdot 10^6$ | Mooring line extensional stiffness $[N/m]$ |
| $40,000$ | Mooring line damping coefficient $[Ns/m]$ |

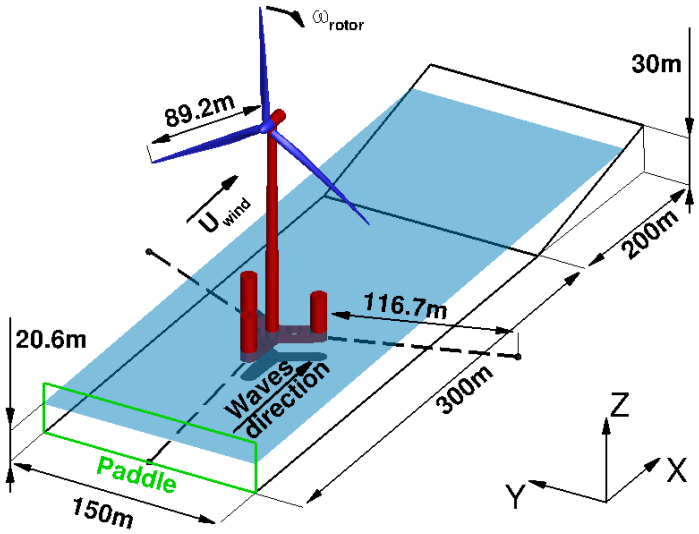


Figure 11: The FOWT model placed in a shallow tank. Mooring lines are shown with dashed lines.

## 4. Results and Discussion

### *4.1. CFD mesh*

The aerodynamic grid consists of the rotor and nacelle *i.e.* the tower is not included (for economies in CPU time) and the effect of the blade passing on the tower is not investigated. The grid consists of $8M$ cells, where 24 cells are used in the boundary layer, and 166 cells are distributed around the aerofoil section as presented in Figure 12b. The surface of the blade is resolved with 90 cells along the span, as shown in Figure 12a.

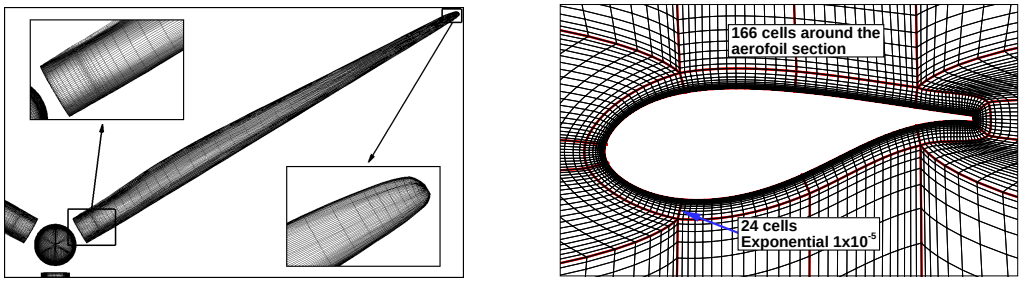


(a) Surface mesh.

(b) Slice close to the blade surface.

Figure 12: $8M$ mesh used to solve for aerodynamic loads. Surface mesh (a), and slice through the volume close to the blade surface (b).

### *4.2. SPH setup and resolution*

The hydrodynamic domain is resolved using $5M$ particles with initial uniform spacing of $d = 0.625m$. Note, that the best agreement with experimental data was obtained for 25 particles per radius of the cylinder, as shown in Section 2.2. Here, the employed spacing corresponds to 9 particles per radius of the cylindrical leg, or to spacing $d = 0.69cm$ in Figure 3b. The coarse particle distribution was chosen for economies in CPU time, where coarse domain is obviously solved faster, but tends to under-predict the slamming loads on the structure. Three test were performed to investigate the influence of the domain width and particle spacing on the force acting on the support structure, as presented in Table 4. The average hydrodynamic forces acting on the support during $1s$ of simulation were used for comparison. Percentage difference is computed relative to the size and spacing employed for the coupled computation. As can be seen, the size of the hydordynamic domain has little effect on the average hydrodynamic force. On the other hand, improving the spatial resolution results in about 18% different hydrodynamic force. This agrees with observations made in Section 2.2. We would have liked to use spacing $d = 0.3125m$, but to improve computational performance we had to employ spacing of $d = 0.625m$.

### *4.3. Initial conditions*

Each of the solvers was executed separately before coupling to obtain a periodic solution of the loads. During this phase of computation the floating support was fixed, and the waves were generated for approximately $30s$. The rotor was computed until the loads converged, and was spinning about the axis aligned with the direction of the incoming wind. Once the initial conditions were obtained, the coupled computations were initiated.

Table 4: Test cases investigating the influence of the domain width and particle spacing on the forces acting on the support structure.

| Domain size $x \times y[m]$ | Spacing $d[m]$ | 1s averaged hydrodynamic force $[N]$ | Difference $[\%]$ |
|---|---|---|---|
| $500 \times 150$ | 0.6250 | $1.070 \cdot 10^7$ | – |
| $500 \times 300$ | 0.6250 | $1.068 \cdot 10^7$ | 0.2% |
| $500 \times 150$ | 0.3125 | $1.267 \cdot 10^7$ | 18.4% |

### *4.4. Test cases*

The first test case consists of the FOWT at the described configuration. Calm sea is considered, and the constant thrust of $1500kN$ is applied at the location of the rotor. A second test case considered time varying rotor thrust as shown in Figure 13. The thrust variation was estimated from a separate CFD computation of the rotor with the tower included. Five Fourier harmonics were used to fit the CFD data. The average thrust over the full revolution was $1500kN$. Both test cases were solved for 150 seconds. Note, that both cases are not coupled simulations, since the thrust force is prescribed and independent of the platform motion. Further, rotor inertia and the associated gyroscopic effects were not taken into account for those cases.

The last test case is a coupled computation, as described in Section 2.5. This case was solved for 60 seconds.

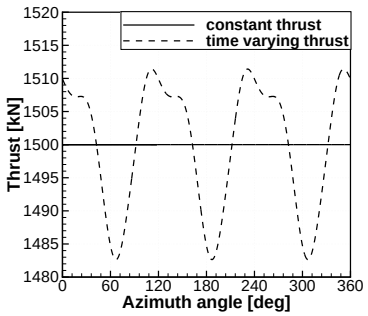


Figure 13: Thrust as function of azimuth angle of the rotor. Two test cases are shown: with constant thrust and estimated time varying thrust.

### *4.5. Decoupled cases - constant and time-varying thrust*

The results of two first cases are presented in Figure 14. As can be seen, the FOWT moves in the direction of the thrust by about $0.215m$ (displacement in $x$). The FOWT also sinks in the water for about $0.603m$ (displacement in $z$), and tends to settle at a pitch angle of around $0.09rad$ or 5.2 degrees (rotation about $y$ axis). The SPH particles are settling for the first 15 seconds as is visible in the acceleration plot. This can not be avoided even if the floating body is fixed and particles are let to settle. This is because releasing the floating structure is equivalent to a drop, and therefore does not represent equilibrium.

Also, the overall response is dominated by the initial imbalance of the forces, and the differences are barely visible in Figure 14.

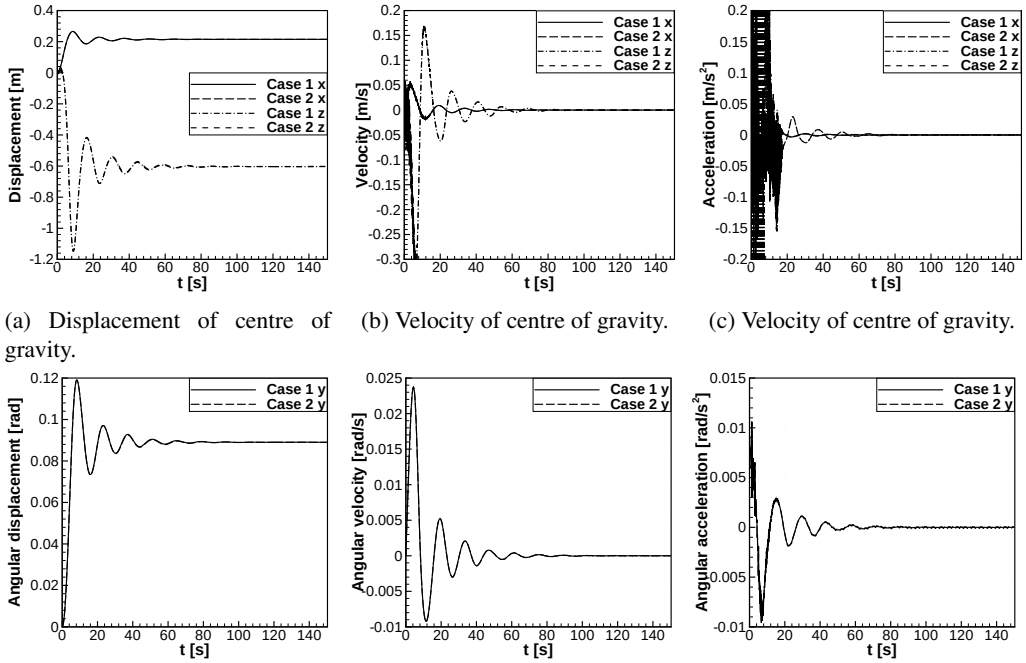


(a) Displacement of centre of gravity.

(b) Velocity of centre of gravity.

(c) Velocity of centre of gravity.

(d) Rotational velocity.

(e) Acceleration of centre of gravity.

(f) Rotational acceleration.

Figure 14: Comparison of lateral and rotational dynamics of the support for two test cases: constant thrust (Case 1) and time varying thrust (Case 2).

The last 20$s$ of lateral and rotational accelerations are presented in Figure 15. The differences for both cases are now clearly visible. The effect of time varying thrust on the angular acceleration in pitch (about $y$ axis) can be seen in Figure 15c, where the variation for the second test case is overlaid on the response for the first case. The variation in the shape and frequency, corresponds to the applied time dependent thrust.

The effect of time varying thrust on the lateral accelerations can be seen in Figure 15. Again, the acceleration in heave (in $z$ direction) for the second test case (constant thrust) is overlaid on the response for the first case (time varying thrust). Here, the frequency of acceleration corresponds to the frequency of the thrust, but some phase shift is present and the shape of the response does not follow the shape of the thrust. This is because the motion in heave is linked to the applied thrust only through the rotational motion of the support i.e. through the second time integral of the angular acceleration, that does follow the shape of the thrust as shown in Figure 15c. The acceleration in the $x$ direction is directly linked to the applied thrust, and the frequency dependence on thrust without the phase shift is clearly visible. However, the shape of the acceleration is not following the shape of applied thrust. This is a result of high stiffness of the mooring lines in this direction, where high frequency response of the mooring system augments the overall response of the support platform.

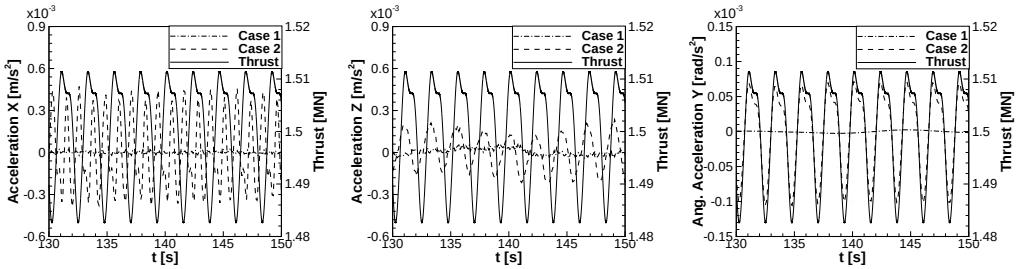


(a) Acceleration of the centre of gravity in surge.

(b) Acceleration of the centre of gravity in heave.

(c) Pitching acceleration about the centre of gravity.

Figure 15: Comparison of last 20 seconds of lateral and rotational accelerations of the support for two test cases: constant thrust (solid line) and time varying thrust (dashed line). Solid line represents time varying thrust, as applied in the second test case.

There are three sources of momentum for the decoupled computations: hydrodynamics, prescribed aerodynamics and mooring lines. Time histories of forces and moments for the test case with constant thrust are presented in Figure 16. Note, that for clarity, the time starts at $20s$. Also, note the differences in magnitude of the computed moments, where moments about $y$ axis are three order of magnitude bigger, as compared to the other moment components.

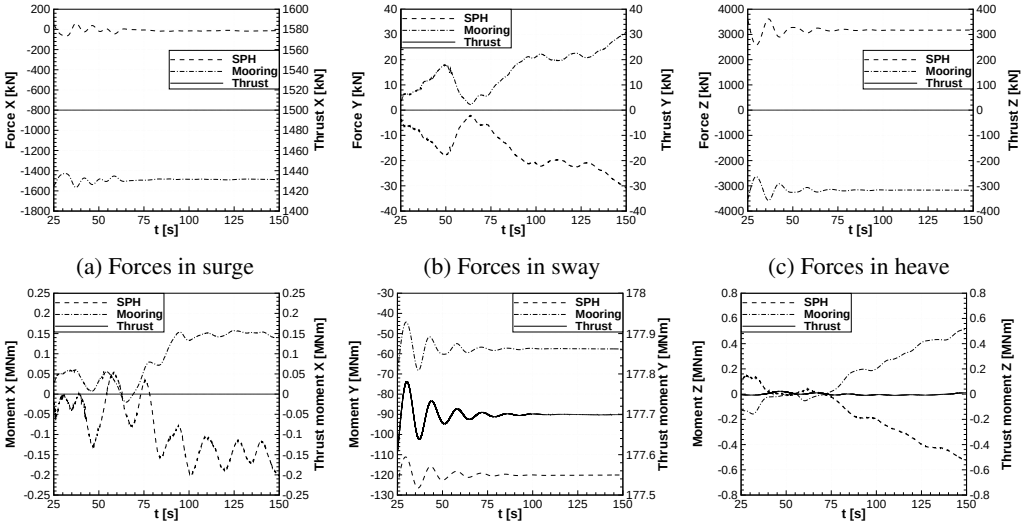


(a) Forces in surge

(b) Forces in sway

(c) Forces in heave

(d) Moments in roll

(e) Moments in pitch

(f) Moments in yaw

Figure 16: Forces and moments acting at CoG of the support for constant thrust case.

First, it should be noted, that mooring lines are in general opposing the hydrodynamic forces introduced by the SPH solver. This is not true for the pitching moment, where hydrodynamics and mooring lines are acting together to counter the imbalance of the moment due to the thrust. For the mooring lines, moment is created by the displacements of the fairleads, whereas for the

hydrodynamics, moment is created by the change of the buoyancy introduced by the rotation of the support. One would expect similar, cooperative behaviour for the forces in surge (in $x$ direction). The obtained results suggest otherwise, as shown in Figure 16a. As can be seen, only the mooring lines are responsible for balancing the thrust force. Since the water is considered calm for the decoupled cases, the only source of hydrodynamic force acting in $x$ direction is the hydrodynamic damping. Therefore, it is acting in the opposite direction of the motion, and as a result in opposite direction to the mooring force, which is a main source of motion in this direction. Lastly, small spurious moments and forces are noted, e.g. force in sway ($y$ direction), which is normal to the plane of symmetry of the support. This is due to the SPH, where motion of the particles is never indeed symmetric. However, these discrepancies diminish with the number of particles, as was seen when test cases from Table 4 were computed. Further, the SPH method is known for its pressure instabilities, where the pressure field of the particles exhibits large pressure oscillations due to acoustic waves present in compressible fluids. This is commonly tackled with solution smoothing techniques, also termed particles smoothing. Schemes up to the second order were proposed in the literature (e.g. Belytschko et al., 2000; Bilotta et al., 2011). In the present work, no particles smoothing was applied, including validation test cases. In fact, stability issues were encountered when a zero-order Shepard density filter was applied to the decoupled test case every 50 and 100 SPH steps.

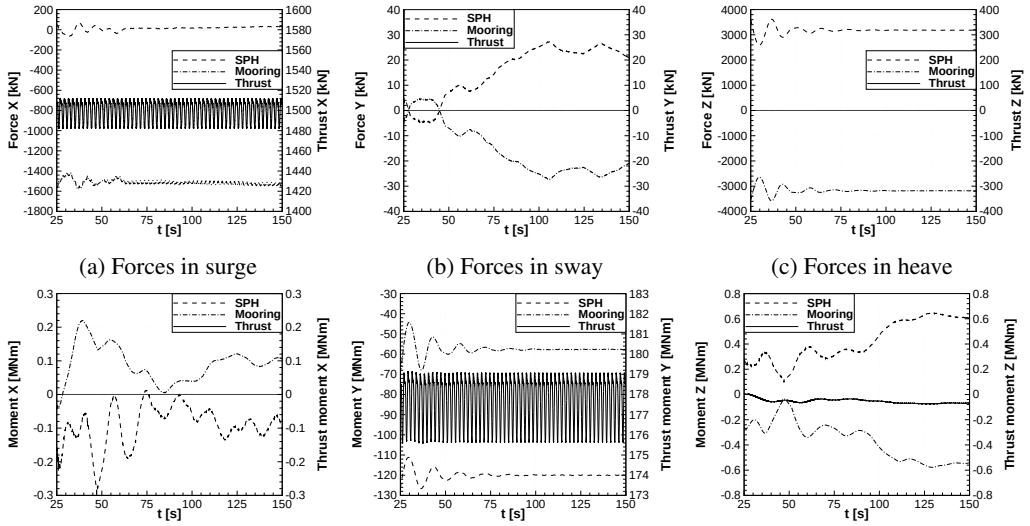


(a) Forces in surge (b) Forces in sway (c) Forces in heave

(d) Moments in roll (e) Moments in pitch (f) Moments in yaw

Figure 17: Forces and moments acting at CoG of the support for time varying thrust case.

The time histories of forces and moments for the second test case with time varying thrust are presented in Figure 17. Visible trends and relations are analogous to the case with constant thrust, and support the observations made in the previous paragraph. The main difference is the expected variation of the forces in surge and moments in pitch, due to the unsteady aerodynamic forcing. Also, hydrodynamic and mooring forces in the $y$ direction changed sign, although the mooring line forces are still opposing the forces of the SPH solver. The same is observed for the moments about $z$ axis. Those quantities are dependent, and opposite rotation creates opposite

mooring line forces.

### *4.6. Coupled case*

Coupled computations were also performed, and results are presented in Figure 18. The aerodynamic forces acting on the rotor as functions of time are shown in Figure 19a. The platform motion shows similar trend as for the previous, decoupled test cases. However, the rotor thrust is now dependent on the position and velocity of the rotor. As the wind turbine pitches under the the thrust force, the rotor moves in the direction of the wind (velocity in $x$ direction in Figure 19b). In return, the thrust force decreases due to the smaller inflow speed and the orientation of the rotor disk. As the applied force is reduced, the rotor velocity decreases. The inverse relation between the aerodynamic force and velocity of the hub in $x$ direction is clear in Figure 19. Further, due to the pitch angle, a component of the thrust is acting along the $z$ axis. As a result, the FOWT experiences higher displacement in heave - $0.8m$ as compared to $0.6m$ for decoupled solutions.

The initial motion of the FOWT is dominated by the imbalance of the forces due to the applied thrust, and the effect of the first wave passage is not visible. However, the effect of every consecutive wave is clearly visible in periodic variation of the moment about the $y$ axis, as shown in Figure 18f.

To facilitate the analysis of forces and moments acting on the system, the aerodynamic moments were transferred to the centre of gravity of the support platform. The resulting time histories of forces and moments for the coupled test case are presented in Figure 20. First, we observe lasting for about $10s$ high frequency hydrodynamic forces and moments due to initial particles settling. Similar was observed for decoupled test cases. After an initial phase, the hydrodynamic forces show periodic variation related to the frequency of the passing waves. Next, the mooring line forces are opposing the SPH forces in all directions. Finally, periodic variation of the aerodynamic forces with frequency of the waves is noted. A phase shift is present, since the aerodynamic forces are dependent on velocity and position, rather than on forces, as was discussed in previous paragraphs.

For the moments, pitching moment (about $y$) is dominating and after the initial phase the solvers tend to a periodic solution. The aerodynamic moment follows the inverse relation to the the hydordynamic pitching moment. The phase shift for the mooring lines moment is present, as it depends on the orientation of the support. The aerodynamic moment about $x$ axis applied at the rotor is a result of a driving force created by the lift. Clearly,the driving force follows the same trend as the thrust force i.e. inverse relation with the velocity of the hub. Part of this moment is transferred to the structure, and hydrodynamic and mooring lines moments are trying to compensate for this moment. Finally, the mooring lines are opposing the hydrodynamic moments for the moment about $z$ axis (yawing).

Figure 21 presents different positions of the FOWT during the computation.

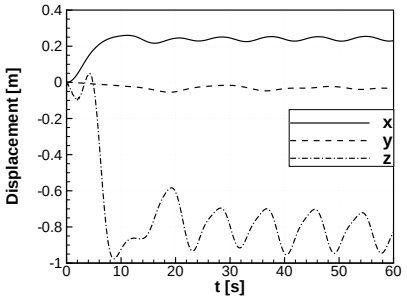


(a) Displacement of centre of gravity.

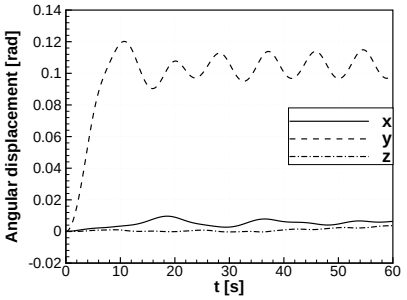


(b) Angular displacement.

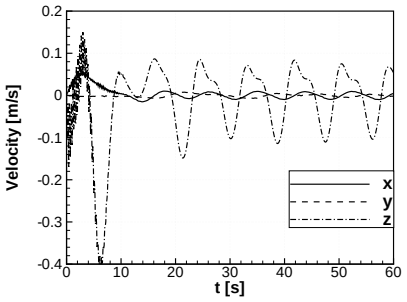


(c) Velocity of centre of gravity.

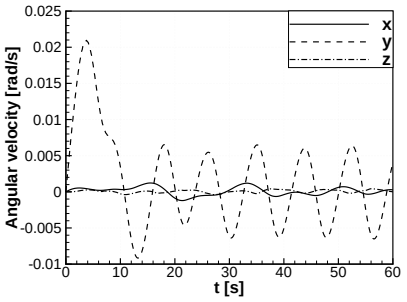


(d) Rotational velocity.

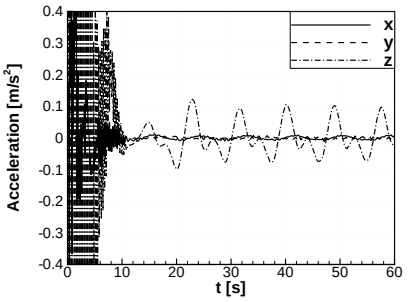


(e) Acceleration of centre of gravity.

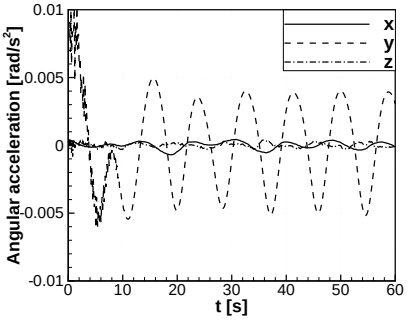


(f) Rotational acceleration.

Figure 18: Lateral and rotational dynamics of the support platform for coupled test case.

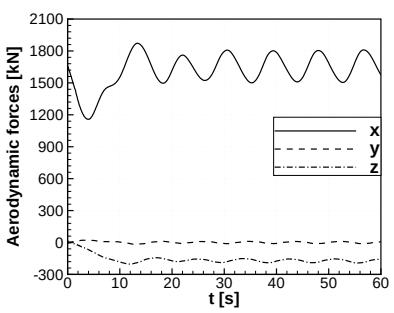


(a) Aerodynamic forces acting on the rotor.

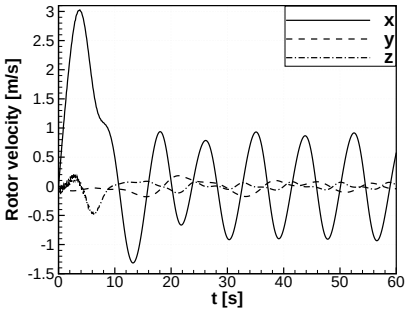


(b) Velocity of centre of gravity of the rotor.

Figure 19: Forces acting on the rotor and velocity of centre of gravity of the rotor as function of time for coupled computation.

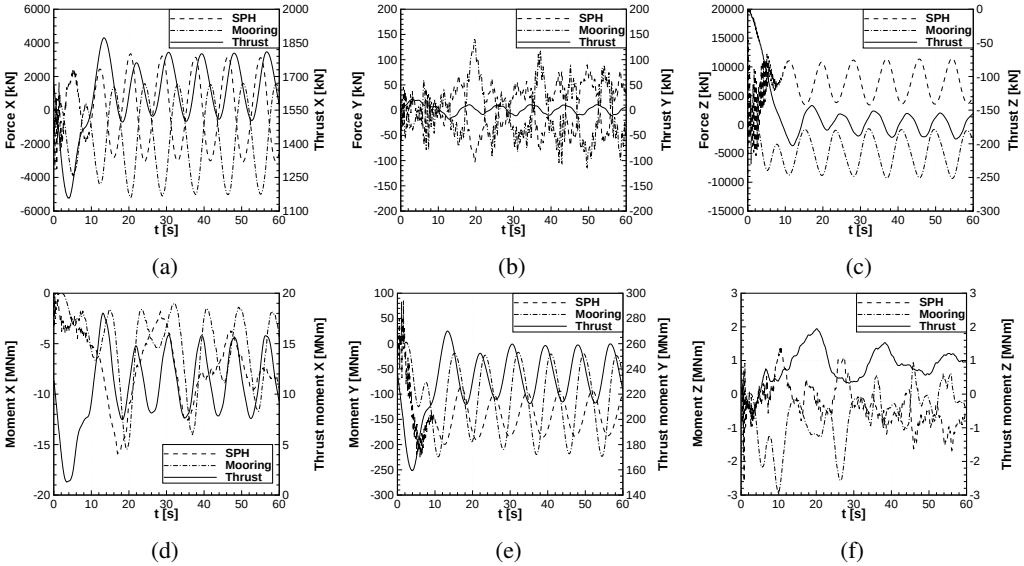


Figure 20: Forces and moments acting at CoG of the support for the coupled test case.

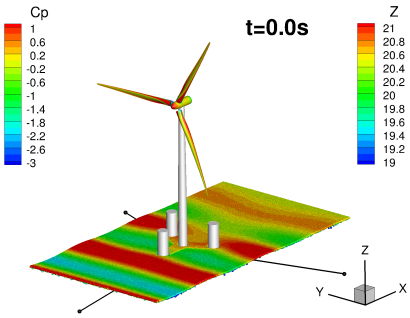


(a) Time $t = 0s$.

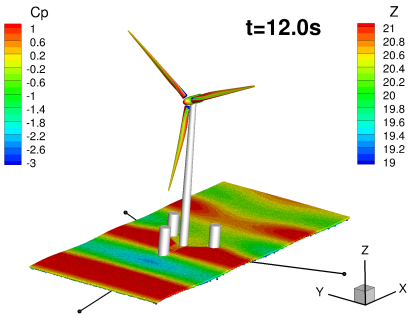


(b) Time $t = 12s$.

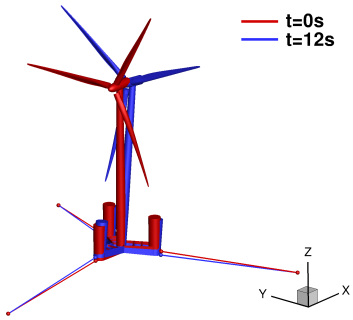


(c) Isometric view of position at times $t = 0s$ and $t = 12s$.

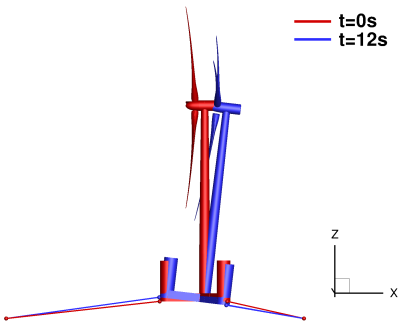


(d) Side view of position at times $t = 0s$ and $t = 12s$.

Figure 21: Position and orientation of the FOWT at times $t = 0s$ and $t = 12s$ during coupled computation. Contours on the rotor correspond to pressure coefficient $Cp$, contours on the water surface correspond to surface elevation $z$ in meters.

*4.7. Computational performance*

For all cases, the SPH solver with MBDM were executed on a single 8 cores Intel®Xeon®CPU machine with 16 threads. Each of the CPU cores had a clock rate of $2GHz$, and $6.6GB$ of dedicated memory. As no interconnect switch was involved, the message passing delay between SPH and MBDM solvers was reduced to minimum. For the coupled case, HMB2 was executed on 29 dual-core AMD Opteron$^{TM}$processors with 4 threads, giving in total 116 parallel instances of the solver. Each of the CPU cores had a clock rate of $2.4GHz$, and $4GB$ of random access memory. It should be noted, that the SPH method requires only local (limited by the kernel function) weighted average in the vicinity of the given particle, whereas HMB2 solves the complete set of equations involving all the cells in the domain. Hence, more processing units were assigned to the aerodynamic side of the coupled problem.

The average time required to compute a second of the solution for the coupled case is 27.26 hours, where about 27.25 hours were spent to solve aerodynamics, 21.3 hours to solve hydrodynamics, and 0.24 hours to solve multi-body equations. The average time spent to exchange information for a second of the solution is 0.53 seconds, and was mostly dictated by the communication between the SPH and the MBDM solvers.

It should be noted, that time accuracy can be improved, if the coupling step is reduced. In the presented coupled case, the information is exchanged every 100 SPH steps ($\Delta t = 2 \cdot 10^{-2}$). When information between the solvers is exchanged every 50 SPH steps ($\Delta t = 1 \cdot 10^{-2}$), the average time required to compute a second of the solution becomes 45.0 hours. If information is exchanged every single SPH step ($\Delta t = 2 \cdot 10^{-4}$), the average time per one second extends to about 438.9 hours. In the former case, HMB2 requires on average 237 pseudo-time steps to achieve the level of convergence below $10^{-2}$, and 45 pseudo-time steps for the later case. The convergence is defined as L2-norm of the residual vector. This suggests, that computational cost can be further reduced by employing explicit schemes for both solvers and performing less evaluations (four for Runge-Kutta scheme of 4th order). However, the biggest possible explicit step for HMB2, that would satisfy explicit CFL condition of 0.4 for the smallest cell in the domain is about $3.6 \cdot 10^{-9}$ seconds. Therefore, the aerodynamic time-step becomes limiting and prohibits this approach. More information about the computational performance is presented in Table 5. Stability issues were encountered for a time step $\Delta t = 2 \cdot 10^{-2}$ and HMB2 implicit CFL number 10.0, where the residual vector does not converge as fast as for CFL number 5.0. This indicates that CFL number of about 8.0 would be an optimal choice for this time step.

Table 5: Computational performance of the coupling algorithm for various coupling time steps.

| Coupling $\Delta t$ [s] | HMB2 CFL number | HMB2 Newton steps | SPH steps | Time per coupling step [s] | Time per 1s of solution [s] |
|---|---|---|---|---|---|
| $2 \cdot 10^{-2}$ | 5.0 | 315 | 100 | $1.95 \cdot 10^{3}$ | $9.81 \cdot 10^{4}$ |
| $2 \cdot 10^{-2}$ | 10.0 | 350 | 100 | $2.29 \cdot 10^{3}$ | $1.15 \cdot 10^{5}$ |
| $1 \cdot 10^{-2}$ | 5.0 | 237 | 50 | $1.61 \cdot 10^{3}$ | $1.62 \cdot 10^{5}$ |
| $1 \cdot 10^{-2}$ | 10.0 | 105 | 50 | $1.04 \cdot 10^{3}$ | $1.06 \cdot 10^{5}$ |
| $2 \cdot 10^{-4}$ | 5.0 | 45 | 1 | $3.13 \cdot 10^{2}$ | $1.58 \cdot 10^{6}$ |
| $2 \cdot 10^{-4}$ | 10.0 | 23 | 1 | $1.59 \cdot 10^{2}$ | $7.97 \cdot 10^{5}$ |

## 5. Conclusions

The paper presented a coupling method for the analysis of off-shore wind turbines. The HMB2 CFD solver was used for the analysis of blade aerodynamics and via a multi-body dynamics method it was coupled to a smoothed particle hydrodynamics tool to model the floating part of the turbine. The results showed that the weak coupling method put forward in this paper is adequate for the solution of the problem at hand. The work suffers from the lack of experimental data for a coupled system and for this reason validation was only possible for the components of the model. Data from the MEXICO project were used for aerodynamics; good overall agreement has been seen between CFD and test data. For the hydrodynamics solver, experiments related to drops of solid objects in water were used. Again, with a refined set of particles, the SPH method delivered good results. The third component of the method was the multi-body dynamics and this was validated using simple slider-crank problems.

Presented results showed that FOWT is a highly dynamic system. To obtain a deeper understanding of how rotor thrust and torque vary under dynamic conditions, efforts should be put forward to study aerodynamic flow and loads when wind turbine undergoes prescribed motion in pitch and yaw. Also, in the future, the work will continue with the validation of the method and comparisons with a strong coupling technique. Another aspect that should be addressed is the experimental measurements. Clearly, each of the components can be validated separately, but the set of comprehensive data for the complete FOWT system is crucial for the model validation. The following measurements would be an asset: forces and moments due to the mooring system, water basin tests with small- or full-scale wind turbine including pressure distributions on support and rotor, and the overall FOWT time responce including transient and periodic states.

## Acknowledgments

The financial support of the Marie Curie Host Fellowships Program: FP7-PEOPLE-2012-ITN-309395 - New Materials And Reliability In Offshore Wind Turbines Technology "MARE-WINT" are gratefully acknowledged.

## References

Bak, C., Zhale, F., Bitsche, R., Kim, T., Yde, A., Henriksen, L. C., Andersen, P. B., Natarajan, A., M.H., H., 2013. Description of the dtu 10 mw reference wind turbin. Technical Report I-0092, DTU Wind Energy.

Barakos, G., Steijl, R., Badcock, K., Brocklehurst, A., 2005. Development of cfd capability for full helicopter engineering analysis. In: 31st European Rotorcraft Forum. Paper No. 91.

Belytschko, T., Guo, Y., Kam Liu, W., Ping Xiao, S., 2000. A unified stability analysis of meshless particle methods. International Journal for Numerical Methods in Engineering 48 (9), 1359–1400.

Bilotta, G., Russo, G., Herault, A., Negro, C. D., 2011. Moving least-squares corrections for smoothed particle hydrodynamics. Annals of Geophysics 54 (5).

Carrión, M., Steijl, R., Woodgate, M., Barakos, G., Munduate, X., Gomez-Iradi, S., 2014. Computational fluid dynamics analysis of the wake behind the mexico rotor in axial flow conditions. Wind Energy.
URL http://dx.doi.org/10.1002/we.1745

Carrión, M., Woodgate, M., Steijl, R., Barakos, G., 2013. Implementation of all-mach roe-type schemes in fully implicit cfd solvers – demonstration for wind turbine flows. International Journal for Numerical Methods in Fluids 73 (8), 693–728.
URL http://dx.doi.org/10.1002/fld.3818

Carrión, M., Woodgate, M., Steijl, R., Barakos, G. N., Gomez-Iradi, S., Munduate, X., 2015. Understanding wind-turbine wake breakdown using computational fluid dynamics. AIAA Journal 53 (3), 588 – 602.

Degroote, J., Haelterman, R., Annerel, S., Bruggeman, P., Vierendeels, J., Apr. 2010. Performance of partitioned procedures in fluid-structure interaction. Computers & Structure 88 (7-8), 446–457.
URL http://dx.doi.org/10.1016/j.compstruc.2009.12.006

Eisenstat, S. C., Elman, H. C., Schultz, M. H., 1983. Variational iterative methods for nonsymmetric systems of linear equations. SIAM Journal on Numerical Analysis 20 (2), 345–357.
URL http://dx.doi.org/10.1137/0720023

Farhat C., van der Zee K.G., Geuzaine P., 2006. Provably second-order time-accurate loosely-coupled solution algorithms for transient nonlinear computational aeroelasticity. Computer Methods in Applied Mechanics and Engineering 195 (1718), 1973 – 2001, fluid-Structure Interaction.

Fellipa C.A., Park K.C., Farhat C., March 1999. Partitioned analysis of coupled mechanical systems. Technical Report CU-CAS-99-06, University of Colorado, Boulder, Colorado, USA.

Fernández, M. A., Moubachir, M., Jan. 2005. A newton method using exact jacobians for solving fluid-structure coupling. Computers & Structure 83 (2-3), 127–142.
URL http://dx.doi.org/10.1016/j.compstruc.2004.04.021

Gomez-Gesteira, M., Rogers, B. D., Crespo, A. J. C., Dalrymple, R. A., Narayanaswamy, M., Dominguez, J. M., Nov. 2012. Sphysics - development of a free-surface fluid solver - part 1: Theory and formulations. Computers & Geosciences 48, 289–299.
URL http://dx.doi.org/10.1016/j.cageo.2012.02.029

Gómez-Iradi, S., Steijl, R., Barakos, G. N., 2009. Development and validation of a cfd technique for the aerodynamic analysis of hawt. Journal of Solar Energy Engineering 131 (3), 031009.

Greenhow, M., Lin, W. M., Sep. 1983. Nonlinear-free surface effects: Experiments and theory. Technical Report 83-19, MIT, Dept. of Ocean Engineering.

Haug, E. J., 1989. Computer Aided Kinematics and Dynamics of Mechanical Systems. Vol. 1: Basic Methods. Allyn & Bacon, Inc., Needham Heights, MA, USA.

Jameson, A., 1991. Time dependent calculations using multigrid, with applications to unsteady flows past airfoils and wings. In: 10th Computational Fluid Dynamics Conference. American Institute of Aeronautics and Astronautics.

Jarkowski, M., Woodgate, M. A., Barakos, G. N., Rokicki, J., 2013. Towards consistent hybrid overset mesh methods for rotorcraft cfd. International Journal for Numerical Methods in Fluids 74 (8), 543–576.
URL http://dx.doi.org/10.1002/fld.3861

Jonkman, J., November 2007. Dynamics modeling and loads analysis of an offshore floating wind turbine. Technical Report NREL/TP-500-41958, NREL.

Karimirad, M., Moan, T., 2012. A simplified method for coupled analysis of floating offshore wind turbines. Marine Structures 27 (1), 45 – 63.

Karimirad, M., Moan, T., 2013. Modeling aspects of a floating wind turbine for coupled wavewind-induced dynamic analyses. Renewable Energy 53, 299–305.

Kttler, U., Wall, W. A., 2008. Fixed-point fluidstructure interaction solvers with dynamic relaxation. Computational Mechanics 43 (1), 61–72.

Larsen, T. J., Hanson, T. D., 2007. A method to avoid negative damped low frequent tower vibrations for a floating, pitch controlled wind turbine. Journal of Physics: Conference Series 75 (1), 012073.

Lee, W. T., Bales, S. L., Sowby, S. E., 1985. Standardized Wind and Wave Environments for North Pacific Ocean Areas. David W. Taylor Naval Ship Research and Development Center.

Leimkuhler, B. J., Reich, S., Skeel, R. D., 1996. Integration methods for molecular dynamics. In: In Mathematical Approaches To Biomolecular Structure And Dynamics, IMA Volumes In Mathematics And Its Applications. Springer, pp. 161–185.

Marino, E., Borri, C., Peil, U., 2011. A fully nonlinear wave model to account for breaking wave impact loads on offshore wind turbines. Journal of Wind Engineering and Industrial Aerodynamics 99 (4), 483 – 490, the Fifth International Symposium on Computational Wind Engineering.

Matha, D., Schlipf, M., Cordle, A., Pereira, R., Jonkman, J., June 2011. Challenges in simulation of aerodynamics, hydrodynamics, and mooring-line dynamics of floating offshore wind turbines. In: 21st Offshore and Polar Engineering Conference.

Nikravesh, P. E., 1988. Computer-aided Analysis of Mechanical Systems. Prentice-Hall, Inc., Upper Saddle River, NJ, USA.

Open MPI, 2015. Open MPI documentation.
URL http://www.open-mpi.org/doc/

Osher, S., Chakravarthy, S., June 1983. Upwind schemes and boundary conditions with applications to euler equations in general geometries. Journal of Computational Physics 50 (3), 447–481.

Rieper, F., Jun. 2011. A low-mach number fix for roe's approximate riemann solver. J. Comput. Phys. 230 (13), 5263–5287.
URL http://dx.doi.org/10.1016/j.jcp.2011.03.025

Roald, L., Jonkman, J., Robertson, A., Chokani, N., 2013. The effect of second-order hydrodynamics on floating offshore wind turbines. Energy Procedia 35, 253 – 264, deepWind'2013 Selected papers from 10th Deep Sea Offshore Wind R&D Conference, Trondheim, Norway, 24 25 January 2013.

Roddier, D., Cermelli, C., Weinstein, A., 2009. WindFloat: A Floating Foundation for Offshore Wind Turbines–Part I: Design Basis and Qualification Process. In: ASME 2009 28th International Conference on Ocean, Offshore and Arctic Engineering. ASME, pp. 845–853.
URL http://dx.doi.org/10.1115/omae2009-79229

Savenije, L. B., Ashuri, T., Bussel, G. J. W., Staerdahl, J. W., 2010. Dynamic modeling of a spar-type floating offshore wind turbine. In: Scientific Proceedings European Wind Energy Conference & Exhibition.

Skaare, B., Hanson, T., Nielsen, F., Yttervik, R., Hansen, A., 2007. Integrated dynamic analysis of floating offshore wind turbines. In: Proceedings of 2007 European Wind Energy Conference and Exhibition.

Spalart, P. R., Jou, W., Strelets, M., Allmaras, S. R., 1997. Comments on the Feasibility of LES for Wings, and on a Hybrid RANS/LES Approach. In: Proceedings of the First AFOSR International Conference on DNS/LES.

Steijl, R., Barakos, G., 2008. Sliding mesh algorithm for cfd analysis of helicopter rotorfuselage aerodynamics. International Journal for Numerical Methods in Fluids 58 (5), 527–549.

Vierendeels, J., Lanoye, L., Degroote, J., Verdonck, P., Jun. 2007. Implicit coupling of partitioned fluid-structure interaction problems with reduced order models. Computers & Structures 85 (11-14), 970–976.

Woodgate, M. A., Barakos, G. N., Scrase, N., Neville, T., September 2013. Simulation of helicopter ditching using smoothed particle hydrodynamics. In: 39th European Rotorcraft Forum.

Zienkiewicz O.C., Taylor R.L., Zhu J.Z., 2005. The Finite Element Method Set (Sixth Edition). Butterworth-Heinemann, Oxford.